Numerical Validation of Composite Panel Impact Tests

Loukham Shyamsunder[1], Bilal Khaled[2], Subramaniam D. Rajan[3], J. Michael Pereira[4], Paul DuBois[5], Gunther Blankenhorn[6]

[1]PhD Student, School of Sustainable Engineering and the Built Environment, Arizona State University, Tempe, AZ

[2]Post-Doctoral Fellow, School of Sustainable Engineering and the Built Environment, Arizona State University, Tempe, AZ

[3]Professor, School of Sustainable Engineering and the Built Environment, Arizona State University, Tempe, AZ. Corresponding author: s.rajan@asu.edu

[4]Research Aerospace Engineer, NASA Glenn Research Center, Cleveland, OH

[5]Research Scientist, George Mason University, Fairfax, VA

[6]Senior R&D Engineer, Ansys-LST, Livermore, CA

Abstract

Researchers have met the challenge of modeling impact events involving composite targets for a variety of applications in a variety of ways. In this paper, the theory and implementation details of an orthotropic visco-elastic-visco-plastic material model with strain rate dependence are discussed. The model is driven by experimental data from quasi-static as well as high strain rate tests, and the data is used in defining the deformation, damage and failure sub-models. Validation data is generated by shooting a hollow 50 g Al-2024 projectile at different velocities against a flat panel target made of unidirectional composite material in a 16-ply $[(0/90/45/-45)_2]_S$ layup. Explicit

dynamic finite element analyses of four high speed tests involving one contained (projectile rebounded) and three uncontained (projectile penetrated) impact tests show that the developed material model and modeling techniques yield reasonable and acceptable predictions.

Keywords

Orthotropic composite, viscoplasticity, impact testing, explicit dynamic finite element analysis

1. Introduction

Researchers have met the challenge of modeling impact events involving composite targets for a variety of applications in a variety of ways. Two of the more common applications can be found in the defense industry [Bhatnagar, 2016; Chen, 2015] and in the aerospace industry [Roberts et al., 2002; Melis et al., 2018]. In these applications, a robust, efficient and easy-to-use numerical modeling scheme is of great importance as it leads to a quicker and reliable design of composite structural systems. For example, development of advanced computational analysis methods was an important aspect of the NASA Advanced Composites Project (ACP) which was created with the goal of reducing the development and certification timeline for new composite structures used in aeronautics applications [Melis et al., 2018]. Development of such a complex framework requires a convergence of several tools – a constitutive model suitable for a wide variety of composite materials and architecture and one that includes deformation, damage and failure components; a versatile explicit dynamics finite element program with capabilities of modeling impact events involving contact, damage, failure and possibly, probabilistic input; a high-fidelity, laboratory-based material characterization process to generate the data for the constitutive model;

and an experimental facility capable of conducting high energy impact testing to create validation data.

Several studies have been conducted in the past where some or all tools needed for impact simulations are discussed. Impact simulations of aircraft engine containment systems involving an aluminum target and a titanium impactor [Ambur et al., 2001], and a Kevlar dry fabric target and a steel impactor [Stahlecker et al., 2009], show the challenges in conducting and modeling the impact event. First, it is difficult to control both the velocity and orientation of the impactor in an experiment. The experience of the laboratory personnel plays an important role and trial-and-error is required especially if specific test data are required, e.g., threshold velocity, V_{50}, etc. Second, constitutive models require several material parameters and sometimes, these are not easy to obtain experimentally. The number of required parameters increases with the increase in sophistication of the model. The simplest orthotropic model in LS-DYNA [Ansys-LST, 2020], *MAT_002 that supports elastic behavior, requires eleven material constants. More sophisticated models that support plastic deformation, damage, rate and temperature sensitivities, and element erosion, may require tens, if not hundreds of material properties. It is challenging first to obtain and then to use these data. To reduce the number of experiments required, there are approaches that can be used to gage the effects of the parameters and rank their importance. For example, first-order sensitivity analysis can be used to gage the effect of individual parameters on the computed response [Stahlecker et al., 2009] and then additional effort can be focused on the more important ones.

While there is no established process to study impact modeling of composite structures, it is recognized that the constituents and the composite architecture play important roles. A healthy

mix of constituent and composite testing along with finite element analysis (FEA) can be used to infer what the behavior of the composite will be at the structural level. A study of non-woven (2D) composite as well as a 3D woven composite with the same constituents (IM7 carbon fibers, CYCOM PR520 epoxy resin matrix) was carried out involving experiments of the material constituents, the composite at low and high strain-rates, and ballistic tests [Chocron et al., 2019]. LS-DYNA mesoscale computer model was developed and used in the numerical simulations. An orthotropic-elastic model was used for the carbon fibers, a Mohr-Coulomb-based material model was used for the matrix, and cohesive mixed mode model was used for the fiber-matrix interface. The authors state that the numerical results indicate that the predictions for the ballistic tests are very good both for ballistic limits and deflections. Not all research solutions require sophisticated models using numerical solution techniques. Researchers [Shaktivesh et al., 2013] have used analytical solution techniques to compute impact-related parameters on a polymer matrix composite target, such as energy absorbed by different mechanisms, kinetic energy of the projectile, contact force, projectile velocity and projectile tip displacement as a function of time.

In Section 2 of the paper, the focus is on modeling impact events using explicit dynamics finite element analysis. A previously developed material model that has been implemented in LS-DYNA as *MAT_213 [Goldberg et al., 2016; Hoffarth et al., 2016; Khaled et al., 2017; Shyamsunder et al., 2019] is suitably modified for modeling impact events over a range of velocities. In the next section, the modeling challenges in impact analysis are discussed with respect to the development and usage of the orthotropic visco-elastic-visco-plastic (VEVP) material model. First, the model enhancement details involving VEVP theory and implementation details are presented. This is followed by specifics of how rate dependent stress-strain data are processed and used. Finally, damage and failure modeling details are discussed to complete the details of the constitutive model.

In the context of this paper, the term *failure onset* implies a reduction in the load carrying capacity, and the term *erosion* implies deletion of elements from the finite element (FE) analysis. The focus of Section 3 is on test setup and data processing of the impact tests. These tests are conducted to generate data for the validation of the developed constitutive model. The target is a 16-ply layup $[(0/90/45/-45)_2]_S$ unidirectional tape made up of T800/F3900 composite material [Toray, 2020] and is impacted by a hollow 50 g Al-2024 projectile. Out of the 14 tests where the projectile speed varied between 119 ft/s to 530 ft/s, simulation of the four highest speed tests involving one contained and three uncontained impact tests are discussed. These tests provide an insight into the accuracy and efficiency of the developed material model. The numerical models and results are discussed in Section 4. The paper concludes with a summary of the performance of the developed model and possible improvements that can be made to the developed constitutive model and modeling process.

2. Modeling Challenges in Impact Analysis

In this section, we discuss three topics alluded to earlier that address the modeling challenges in impact of composite panels. The first topic is enhancing the capabilities of MAT_213 by modifying the deformation model to be able to capture visco-elastic and visco-plastic behaviors. The second topic deals with pre-processing stress-strain curves corresponding to different strain-rates to yield consistent data for use by the constitutive model. The last topic deals with incorporating damage and failure models in the constitutive model framework thus providing the means to track the behavior of the target composite structure for both contained and uncontained impacts.

2.1 Overview of Material Model

Experiments have shown that (a) structural composites exhibit nonlinear stress-strain response both when loaded and unloaded with the unload slope decreasing with increasing strain, and (b) the overall response including initial elastic modulus change with strain rate [Daniel et al., 2011; Khaled et al., 2017; Deshpande et al., 2019]. Examples of stress-strain curves at several strain rates and room temperature for a carbon fiber reinforced polymer composite, T800/F3900 [Toray, 2020] used for the validation tests in the paper are shown in Fig. 1.

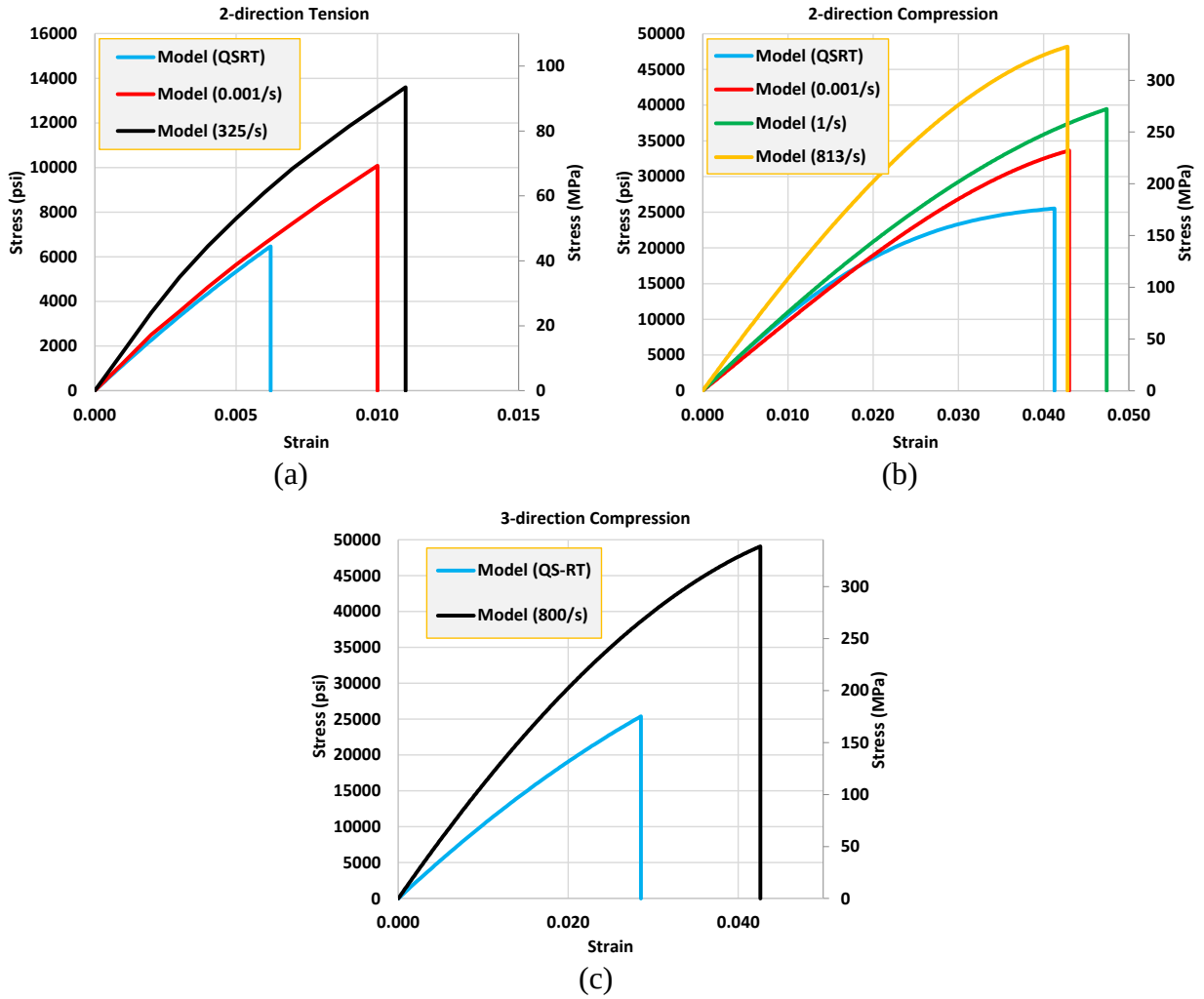

Figure 1. Stress-strain curves for (a) 2-direction tension (b) 2-direction compression (c) 3-direction compression ("1" is along the fiber direction, "2" and "3" refer to the transverse in-plane and through-thickness directions. QS-RT denotes quasi-static room temperature.

"Model" denotes average of several test replicates.) [Khaled et al., 2017; Deshpande et al., 2019]

The stress-strain curves shown in Fig. 1 were generated from physical test of coupons obtained from multi-ply unidirectional composite panels. There are two approaches to developing a material model to capture the nonlinear behavior – continuum damage mechanics models [Matzenmiller et al., 1995; Maimi et al., 2007; Wu and Yao, 2010] and plasticity [Sun and Chen, 1989; Vaziri et al, 1991; Khan and Huang, 1995; Cho et al., 2010]. In the present work, the constitutive model is divided into three sub-models – deformation [Goldberg et al., 2016] damage [Khaled et al., 2019a] and failure [Goldberg et al., 2018; Shyamsunder et al., 2019, 2020b]. Adding the visco-elastic component to the material model facilitates modeling rate-dependent behavior of the material in the elastic regime in a physically consistent manner, whereas the visco-plastic component is used to capture the strain-rate effects in the plastic domain which accounts for the permanent deformation. The combination of the visco-elastic and the visco-plastic approach is referred here to as visco-elastic-visco-plastic (VEVP) model. The VEVP behavior is captured in the deformation sub-model. A yield function which is a modified form of the commonly used Tsai–Wu composite failure model is used as

$$f(\sigma) = a + \begin{pmatrix} F_1 & F_2 & F_3 & 0 & 0 & 0 \end{pmatrix} \begin{bmatrix} \sigma_{11} \\ \sigma_{22} \\ \sigma_{33} \\ \sigma_{12} \\ \sigma_{23} \\ \sigma_{31} \end{bmatrix} + \begin{bmatrix} \sigma_{11} \\ \sigma_{22} \\ \sigma_{33} \\ \sigma_{12} \\ \sigma_{23} \\ \sigma_{31} \end{bmatrix}^T \begin{bmatrix} F_{11} & F_{12} & F_{13} & 0 & 0 & 0 \\ F_{12} & F_{22} & F_{23} & 0 & 0 & 0 \\ F_{13} & F_{23} & F_{33} & 0 & 0 & 0 \\ 0 & 0 & 0 & F_{44} & 0 & 0 \\ 0 & 0 & 0 & 0 & F_{55} & 0 \\ 0 & 0 & 0 & 0 & 0 & F_{66} \end{bmatrix} \begin{bmatrix} \sigma_{11} \\ \sigma_{22} \\ \sigma_{33} \\ \sigma_{12} \\ \sigma_{23} \\ \sigma_{31} \end{bmatrix} \quad (1)$$

where $a = -1$. The yield function coefficients, F_i and F_{ij}, depend on the current yield stress values and are calculated as

$$F_1 = \frac{1}{\sigma_{11}^T} - \frac{1}{\sigma_{11}^C} \qquad F_{11} = \frac{1}{\sigma_{11}^T \sigma_{11}^C} \qquad F_{44} = \frac{1}{\sigma_{12}^2}$$
$$F_2 = \frac{1}{\sigma_{22}^T} - \frac{1}{\sigma_{22}^C} \qquad F_{22} = \frac{1}{\sigma_{22}^T \sigma_{22}^C} \qquad F_{55} = \frac{1}{\sigma_{23}^2} \tag{2}$$
$$F_3 = \frac{1}{\sigma_{33}^T} - \frac{1}{\sigma_{33}^C} \qquad F_{33} = \frac{1}{\sigma_{33}^T \sigma_{33}^C} \qquad F_{66} = \frac{1}{\sigma_{31}^2}$$

$$F_{12} = \frac{2}{\left(\sigma_{12}^{45}\right)^2} - \frac{F_1 + F_2}{\sigma_{12}^{45}} - \frac{1}{2}\left(F_{11} + F_{22} + F_{44}\right)$$
$$F_{23} = \frac{2}{\left(\sigma_{23}^{45}\right)^2} - \frac{F_2 + F_3}{\sigma_{23}^{45}} - \frac{1}{2}\left(F_{22} + F_{33} + F_{55}\right) \tag{3}$$
$$F_{13} = \frac{2}{\left(\sigma_{31}^{45}\right)^2} - \frac{F_1 + F_3}{\sigma_{31}^{45}} - \frac{1}{2}\left(F_{11} + F_{33} + F_{66}\right)$$

where the superscripts T, C and 45 denote data obtained from tension, compression and 45-degree off-axis tests, respectively. The plastic potential function used with a non-associative flow rule is defined as

$$h = \sqrt{\begin{matrix} H_{11}\sigma_{11}^2 + H_{22}\sigma_{22}^2 + H_{33}\sigma_{33}^2 + 2H_{12}\sigma_{11}\sigma_{22} + 2H_{23}\sigma_{22}\sigma_{33} + 2H_{31}\sigma_{33}\sigma_{11} \\ + H_{44}\sigma_{12}^2 + H_{55}\sigma_{23}^2 + H_{66}\sigma_{31}^2 \end{matrix}} \tag{4}$$

where the H_{ij} terms are a set of constant coefficients which are computed based on the plastic Poisson's ratios, with the coefficients (referred to as flow rule coefficients) defined as input parameters in the model [Hoffarth et al., 2017]. Plasticity has been used to capture nonlinearity in a phenomenological fashion in order to capture the permanent strains in addition to accounting for strain rate effects in a physically consistent manner.

The damage sub-model is used for two purposes. First, the damage sub-model, which is synergistic to the plasticity model, tracks the reduction in the unloading slope that takes place with increasing plastic strain. A semi-coupled damage model is used to account for the fact that loading in one direction can lead to stiffness reductions in other material directions. Fig. 2 shows an example

stress-strain curve from the in-plane shear test with a cyclic displacement-controlled loading. Damage-related parameters are obtained from this test.

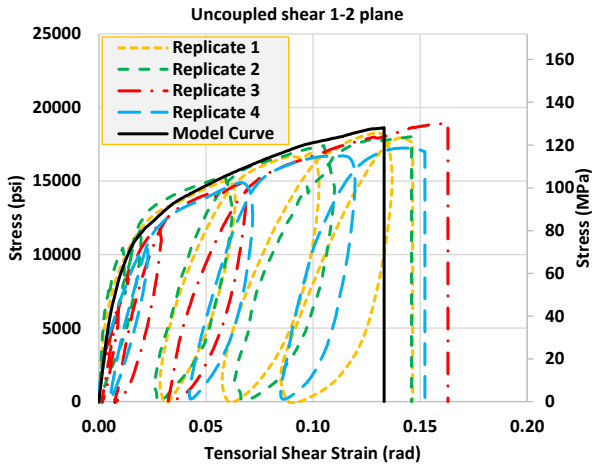

Figure 2. 1-2 shear specimen subjected to cyclic loading [Khaled et al., 2017, 2019a]

While the deformation sub-model provides the mechanism to simulate the nonlinear stress-strain response, the damage sub-model is used to capture nonlinear unloading and local plastic softening often observed in composites [Barbero, 2013; Goldberg et al., 2016]. In our earlier work [Goldberg et al., 2018], we show that using the strain equivalence assumption specifies that the effective stresses result in the same deformations in the effective, undamaged material as would be caused by applying the actual stresses on the damaged material. In this way, the yield function, flow rule, and constitutive equation, can be written in terms of the effective stresses and applied in effective stress space. The use of effective stresses allows the plasticity calculations to be uncoupled from the damage law.

Second, the damage sub-model, as shown later, is used to permit the simulation of post-peak stress degradation that is required to account for the load shedding that takes place in actual materials and mitigates the potential of a sudden brittle failure being simulated once the peak stress is reached in the simulation of impact events.

Finally, the failure sub-model is used to erode the element when the erosion strain is reached. The motivation for using the generalized tabulated failure model is to allow the failure surface to take on any arbitrary shape and not be driven by specific geometrical shapes defined by mathematical equations. This point cloud of failure surface associated with composites permits complex loading scenarios to be handled correctly, e.g., permitting tension-compression asymmetry, shear-dominated failure, etc. The input needed to drive the material model includes the following: (a) at a minimum, twelve sets of stress-strain curves at a specified temperature-strain rate combination (3 tension tests in the principal material directions (PMDs), 3 compression tests in the PMDs, 3 shear tests in the principal material planes, and 3 45^0 off-axis tests) which are input as tabulated data set, (b) damage model-related data obtained from coupled and uncoupled damage tests in the PMDs [Khaled et al., 2019a], and (c) additional data that include mass density, elastic orthotropic material properties, flow rule coefficients, VEVP related parameters, and failure model-related parameters.

2.2 Visco-elastic-visco-plastic Considerations

The VEVP behavior can be represented as a spring-dashpot model as shown in Fig. 3. To derive the stresses in the visco-elastic and the visco-plastic component, the model shown in Fig. 3 can be divided into a standard linear solid model and a hardening model, separately. There are at least three different approaches to viscoplasticity [Wang et al., 1997] – overstress visco-plastic models of Perzyna and of Duvaut-Lions, and the consistency visco-plastic approach. In the present work, the consistency approach is used since only with this approach it is possible to use the Kuhn-Tucker form of the loading-unloading conditions in the visco-plastic case.

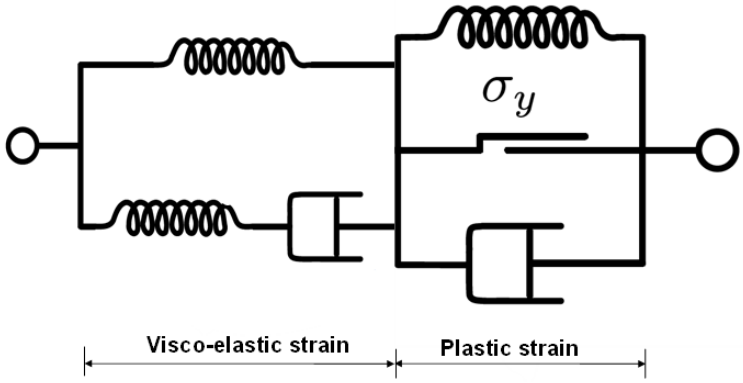

194

195 **Figure 3. Schematic of VEVP model**
196

197 The stress is divided into equilibrium, $\boldsymbol{\sigma}_{n+1}^{e,eff}$ and viscous, $\boldsymbol{\sigma}_{n+1}^{v,eff}$ components [Du Bois et al., 2017;

198 Achstetter, 2019] that are computed as

199 $$\boldsymbol{\sigma}_{n+1}^{e,eff} = \boldsymbol{\sigma}_{n}^{e,eff} + \mathbf{C}_{\infty}\dot{\boldsymbol{\varepsilon}}_{n+1}^{avg}\Delta t \tag{5}$$

200 $$\boldsymbol{\sigma}_{n+1}^{v,eff} = \boldsymbol{\sigma}_{n}^{v,eff} \circ \boldsymbol{\beta} + \left[\left(\mathbf{C} - \mathbf{C}_{\infty}\right) \circ \mathbf{B}\right]\dot{\boldsymbol{\varepsilon}}_{n+1}^{avg}\Delta t \tag{6}$$

201 where $\circ$ denotes Hadamard product between the matrices or vectors. These computations take

202 place in the effective stress space [Khaled et al., 2019a] and hence the superscript *eff* is used. $\mathbf{C}_{\infty}$

203 is the equilibrium stiffness matrix generated using the moduli corresponding to the quasi-static

204 stress-strain curves while $\mathbf{C}$ is the total stiffness matrix generated using the moduli corresponding

205 to the current strain rate. In computing the total stiffness matrix, the total strain-rate, $\dot{\boldsymbol{\varepsilon}}_{n+1}^{avg}$ and the

206 temperature is used to determine the moduli for a given time step and Gauss point [Shyamsunder

207 et al., 2020a]. It is necessary to smoothen out the strain-rate components to avoid numerical

208 instabilities. This is done using an exponential averaging technique as

209 $$\dot{\boldsymbol{\varepsilon}}_{n+1}^{avg} = (1 - FILT) \times \dot{\boldsymbol{\varepsilon}}_{n+1} + FILT \times \dot{\boldsymbol{\varepsilon}}_{n}^{avg} \tag{7}$$

210 where n denotes the previous time step, and $0 \le FILT \le 1$. Using Eq. 7, the average strain rates at

211 the current time step, $\dot{\boldsymbol{\varepsilon}}_{n+1}^{avg}$ are computed as a function of the non-smooth strain rates at the current

time step, $\dot{\boldsymbol{\varepsilon}}_{n+1}$ and the averaged strain rate from the previous time step, $\dot{\boldsymbol{\varepsilon}}_n^{avg}$. Vector $\boldsymbol{\beta}$ and the matrix $\mathbf{B}$ are given by the following expressions [Achstetter, 2019]

$$\boldsymbol{\beta} = \begin{bmatrix} e^{-\beta_{11}\Delta t} & e^{-\beta_{22}\Delta t} & e^{-\beta_{33}\Delta t} & e^{-\beta_{44}\Delta t} & e^{-\beta_{55}\Delta t} & e^{-\beta_{66}\Delta t} \end{bmatrix}^T \tag{8}$$

$$\mathbf{B} = \begin{bmatrix} \frac{1-e^{-\beta_{11}\Delta t}}{\beta_{11}\Delta t} & \frac{1-e^{-\beta_{12}\Delta t}}{\beta_{12}\Delta t} & \frac{1-e^{-\beta_{13}\Delta t}}{\beta_{13}\Delta t} & 0 & 0 & 0 \\ \frac{1-e^{-\beta_{12}\Delta t}}{\beta_{12}\Delta t} & \frac{1-e^{-\beta_{22}\Delta t}}{\beta_{22}\Delta t} & \frac{1-e^{-\beta_{23}\Delta t}}{\beta_{23}\Delta t} & 0 & 0 & 0 \\ \frac{1-e^{-\beta_{13}\Delta t}}{\beta_{13}\Delta t} & \frac{1-e^{-\beta_{23}\Delta t}}{\beta_{23}\Delta t} & \frac{1-e^{-\beta_{33}\Delta t}}{\beta_{33}\Delta t} & 0 & 0 & 0 \\ 0 & 0 & 0 & \frac{1-e^{-\beta_{44}\Delta t}}{\beta_{44}\Delta t} & 0 & 0 \\ 0 & 0 & 0 & 0 & \frac{1-e^{-\beta_{55}\Delta t}}{\beta_{55}\Delta t} & 0 \\ 0 & 0 & 0 & 0 & 0 & \frac{1-e^{-\beta_{66}\Delta t}}{\beta_{66}\Delta t} \end{bmatrix} \tag{9}$$

where, β_{ij}'s, $ij = 11, 22, 33, 44, 55, 66, 12, 23$ and 13, are the decay constants. Currently, there are no experimental methods to determine these β_{ij} values. These β_{ij} parameters are fitted in such a way that together with the tabulated definition of the rate dependent Young's modulus, they allow to simulate the rate dependent slopes of the stress-strain curves measured in the experiments. It should be noted here that the visco-elastic model that is used is highly non-linear since linear viscoelasticity will not allow to fit the initial slopes for a wide enough range of strain rates. The β_{ij} parameters should be small enough not over damp and large enough to allow for viscoelasticity. Typically, a trial-and-error process is carried out to estimate these values, e.g., inverse analysis. The components of $\boldsymbol{\sigma}_n^{e,eff}$ and $\boldsymbol{\sigma}_n^{v,eff}$ are given by the following equations

$$\sigma_{11,n}^{i,eff} = \begin{cases} \dfrac{\sigma_{11,n}^{i}}{1-c_1^d} & if\ \sigma_{11,n} \geq 0 \\ \dfrac{\sigma_{11,n}^{i}}{1-c_4^d} & if\ \sigma_{11,n} < 0 \end{cases} \quad (10)$$

$$\sigma_{22,n}^{i,eff} = \begin{cases} \dfrac{\sigma_{22,n}^{i}}{1-c_2^d} & if\ \sigma_{22,n} \geq 0 \\ \dfrac{\sigma_{22,n}^{i}}{1-c_5^d} & if\ \sigma_{22,n} < 0 \end{cases} \quad (11)$$

$$\sigma_{33,n}^{i,eff} = \begin{cases} \dfrac{\sigma_{33,n}^{i}}{1-c_3^d} & if\ \sigma_{33,n} \geq 0 \\ \dfrac{\sigma_{33,n}^{i}}{1-c_6^d} & if\ \sigma_{33,n} < 0 \end{cases} \quad (12)$$

$$\sigma_{12,n}^{i,eff} = \frac{\sigma_{12,n}^{i}}{1-c_7^d} \quad (13)$$

$$\sigma_{23,n}^{i,eff} = \frac{\sigma_{23,n}^{i}}{1-c_8^d} \quad (14)$$

$$\sigma_{13,n}^{i,eff} = \frac{\sigma_{13,n}^{i}}{1-c_9^d} \quad (15)$$

where, i can be either e (equilibrium) or v (viscous) and the stress components on the right-hand side are in the true stress space. An assumption is thus made that damage affects the equilibrium and viscous stresses in the same way. The true stress space corresponds to the damaged state whereas the effective space corresponds to the undamaged state. Strain equivalence assumption allows the damage sub-model to predict the reduction in the stiffness without affecting the deformation sub-model. The parameter, c_i^d, is referred to as the effective damage parameter and is a measure of damage in each component in the principal material direction/plane [Shyamsunder et al., 2020b]. These are given by the following expressions for the normal component,

$$c_i^d = 1-\left\{\left(1-d_{11_T}^{ii_T}\right)\left(1-d_{11_C}^{ii_T}\right)\left(1-d_{22_T}^{ii_T}\right)\left(1-d_{22_C}^{ii_T}\right)\left(1-d_{33_T}^{ii_T}\right)\left(1-d_{33_C}^{ii_T}\right)\left(1-d_{12}^{ii_T}\right)\left(1-d_{23}^{ii_T}\right)\left(1-d_{13}^{ii_T}\right)\right\} \quad (16)$$

$$c_{i+3}^d = 1-\left\{\left(1-d_{11_T}^{ii_C}\right)\left(1-d_{11_C}^{ii_C}\right)\left(1-d_{22_T}^{ii_C}\right)\left(1-d_{22_C}^{ii_C}\right)\left(1-d_{33_T}^{ii_C}\right)\left(1-d_{33_C}^{ii_C}\right)\left(1-d_{12}^{ii_C}\right)\left(1-d_{23}^{ii_C}\right)\left(1-d_{13}^{ii_C}\right)\right\} \quad (17)$$

where i = 1, 2 and 3. The shear components are given as

236
$$c_k^d = 1 - \left\{ \left(1 - d_{11_T}^{ij}\right)\left(1 - d_{11_C}^{ij}\right)\left(1 - d_{22_T}^{ij}\right)\left(1 - d_{22_C}^{ij}\right) \left(1 - d_{33_T}^{ij}\right)\left(1 - d_{33_C}^{ij}\right)\left(1 - d_{12}^{ij}\right)\left(1 - d_{23}^{ij}\right)\left(1 - d_{13}^{ij}\right) \right\} \quad (18)$$

237 where, ij =12, 23 and 13, and k = 7, 8 and 9, respectively. d_{ij}^{kl} is referred to as the damage
238 parameter and accounts for damage in the kl direction due to loading in the ij direction. If the ij
239 direction and the kl direction are the same, d_{ij}^{kl} is referred to as an uncoupled damage parameter.
240 Otherwise, it is referred to as coupled damage parameter. For example, in Eq. 16, $d_{22_T}^{22_T}$ is an
241 uncoupled damage parameter obtained by loading the specimen in 2-direction tension and
242 interrogating the reduction in stiffness in the 2-direction tension. Similarly, $d_{22_C}^{22_T}$ is a coupled
243 damage parameter obtained by loading the specimen in 2-direction compression and interrogating
244 the reduction in the stiffness in the 2-direction tension. The conversion from the true stress space
245 to the effective stress space is done separately for the equilibrium and the viscous components.
246 The components of $\boldsymbol{\sigma}_n^{v,eff}$ are taken as zero if the material is assumed to be purely visco-plastic.
247 The total trial stress is computed using the following equation

248
$$\boldsymbol{\sigma}_{n+1}^{t,eff} = \boldsymbol{\sigma}_{n+1}^{e,eff} + \boldsymbol{\sigma}_{n+1}^{v,eff} \quad (19)$$

249 The total trial stress is corrected back to the yield surface using a radial return algorithm. The yield
250 function given by Eq. 1 is computed based on the total trial stress, $f(\boldsymbol{\sigma}_{n+1}^{t,eff})$. It has to be noted that
251 the yield function coefficients (F_i and F_{ij}) are computed based on the current yield stresses
252 corresponding to the quasi-static stress-strain curves to predict the onset of plasticity [Hoffarth et
253 al., 2016]. The stress tensor in the effective space is updated as

254
$$\boldsymbol{\sigma}_{n+1}^{eff} = \left(\boldsymbol{\sigma}_{n+1}^{t,eff} - \left[\mathbf{C}_\infty + \left(\mathbf{C} - \mathbf{C}_\infty \right) \circ \mathbf{B} \right] \Delta\lambda \left. \frac{\partial h}{\partial \boldsymbol{\sigma}} \right|_{\boldsymbol{\sigma}_{n+1}^{t,eff}} \right) \quad (20)$$

where, $\Delta\lambda$ is the plastic multiplier and is taken as zero if the material is assumed to be purely visco-elastic, and h is the plastic potential function given by Eq. 4. For a given simulation, the user input is pre-processed where for each input stress-strain curve, the stress is converted into effective stress, and the strain is converted into plastic strain and finally to effective plastic strain (illustrated in Fig. 4). Each of these curves is assigned an effective plastic strain rate which is computed based on the strain-rate specified for each input curves. During the simulation, $\Delta\lambda$ is computed as a function of the current yield stress obtained from interpolation using the effective plastic strain rate and the temperature. The highest and the lowest rate curves are used if the current value is greater than or less than the given user input curves. It should be noted that even though the implementation supports user input for stress-strain curves at various strain-rate and temperature combinations, only strain-rate has been varied in the current work. The authors do not yet have experimental data for loading and unloading at different combinations of strain-rate and temperature. After the stress is updated using Eq. 20, the equilibrium and the viscous stresses also need to be updated. In order to ensure that the total stress is equal to the sum of the equilibrium and the viscous stresses, these stress tensors are updated as follows:

If $f(\boldsymbol{\sigma}_{n+1}^{e,eff}) \le \delta_{tol}$,

$$\boldsymbol{\sigma}_{n+1}^{e,eff} = \boldsymbol{\sigma}_{n+1}^{e,eff} \tag{21}$$

$$\boldsymbol{\sigma}_{n+1}^{v,eff} = \boldsymbol{\sigma}_{n+1}^{v,eff} - \left[\mathbf{C}_{\infty} + \left(\mathbf{C} - \mathbf{C}_{\infty}\right) \circ \mathbf{B}\right] \Delta\lambda \left.\frac{\partial h}{\partial \boldsymbol{\sigma}}\right|_{\boldsymbol{\sigma}_{n+1}^{t,eff}} \tag{22}$$

else

$$\boldsymbol{\sigma}_{n+1}^{e,eff} = \left(\boldsymbol{\sigma}_{n+1}^{e,eff} - \mathbf{C}_{\infty} \Delta\lambda \left.\frac{\partial h}{\partial \boldsymbol{\sigma}}\right|_{\boldsymbol{\sigma}_{n+1}^{t,eff}} \right) \tag{23}$$

$$\boldsymbol{\sigma}_{n+1}^{v,eff} = \boldsymbol{\sigma}_{n+1}^{v,eff} - \left[\left(\mathbf{C} - \mathbf{C}_{\infty}\right) \circ \mathbf{B}\right] \Delta\lambda \left.\frac{\partial h}{\partial \boldsymbol{\sigma}}\right|_{\boldsymbol{\sigma}_{n+1}^{t,eff}} \tag{24}$$

where δ_{tol} is a tolerance used in the analysis, which for the current work is taken as 10^{-6}. Eqs. 21-24 show that if the yield function value computed from the equilibrium stress is non-positive, the return to the yield surface is achieved by reducing the viscous stresses only. This ensures that the stress does not fall below the equilibrium stress in the effective space. Finally, $\boldsymbol{\sigma}_{n+1}^{eff}$, $\boldsymbol{\sigma}_{n+1}^{e,eff}$ and $\boldsymbol{\sigma}_{n+1}^{v,eff}$ are converted into the true stress space using Eqs. 10-15. The updated $\boldsymbol{\sigma}_{n+1}^{e,eff}$ and $\boldsymbol{\sigma}_{n+1}^{v,eff}$ are used in the next time step for computation of trial stress.

2.3 Processing Rate Data

Careful processing of rate-dependent stress-strain data before it is used in finite element analysis is necessary to ensure that the data for various rates are used consistently in the constitutive model. Input to the material law consists of yield curves corresponding to different values of the equivalent plastic strain rates. The difference in yield stress between two curves corresponds to viscous stress. For a positive increment of the equivalent plastic strain rate the effective viscous stress increment must be positive, as viscosity is necessarily positive. Consequently, yield curves at higher strain rates must necessarily be above yield curves at lower strain rates. And yield curves at different strain rates cannot intersect.

Processing of the input stress-strain curves is illustrated using Fig. 1(a) and Fig. 4 as an example. The term *QS-RT* refers to testing carried out at quasi-static (~10^{-4}/s), room temperature conditions, and *Model* refers to the curve generated from the average values obtained from multiple test replicates and used as input to the constitutive model. Fig. 1(a) shows the curves for the 2-direction

tension component at three different strain rates [Khaled et al., 2017; Deshpande et al., 2019]. The corresponding effective stress-effective plastic strain curves are shown in Fig. 4. Care must be taken to avoid intersecting effective stress-effective plastic strain curves as intersecting curves will likely result in either inaccurate results or numerical instability. Often, intersecting curves result from selecting an incorrect initial yield strain value.

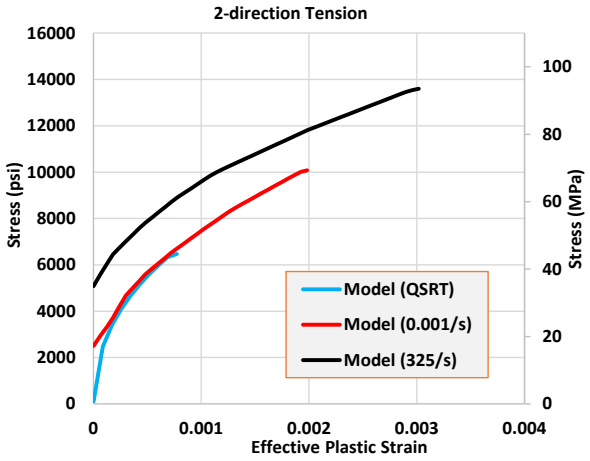

Figure 4. Effective stress versus effective plastic strain curves for 2-direction tension data for the T800-F3900 composite constructed from data in Fig. 1(a).

2.4 Failure Modeling

A failure model where an arbitrarily shaped failure surface in the stress space can be used to predict the failure of a composite is highly desirable [Goldberg et al., 2018]. In this paper, the Generalized Tabulated Failure Criterion (GTFC) implemented in MAT_213 is used [Shyamsunder et al., 2020b]. The current implementation is designed for unidirectional, laminated composites. The failure state is divided into two components– in-plane failure taking place in the 1-2 plane and out-of-plane failure involving the out-of-plane stress/strain components. Failure surfaces need to be defined for each of these failure states in the equivalent failure strain and failure angle space. Fig.

5 shows the in-plane failure surface where $\varepsilon_{IP^{FAIL}}^{eq}$ is a function of the failure angle, θ_{IP}. It must be noted that the term failure angle is unrelated to the fracture plane angle in a composite. The data to construct this surface can be obtained from laboratory testing or from virtual testing. Typically, the testing process starts with uniaxial testing in the 1- and in the 2-directions with tensile and compressive loadings, and a pure shear test. This would yield the final states of stress and strain (ignoring relatively small magnitudes) as $\left(\sigma_1^t,0,0\right)$, $\left(\sigma_2^t,0,0\right)$, $\left(\sigma_1^c,0,0\right)$, $\left(\sigma_2^c,0,0\right)$, $\left(\varepsilon_1^t,0,0\right)$, $\left(\varepsilon_2^t,0,0\right)$, $\left(\varepsilon_1^c,0,0\right)$, $\left(\varepsilon_2^c,0,0\right)$, $\left(0,0,\sigma_{12}\right)$, and $\left(0,0,\varepsilon_{12}\right)$. This can be followed by biaxial testing (laboratory or virtual) yielding a richer set of $\left(\sigma_1,\sigma_2,\sigma_{12}\right)$ and $\left(\varepsilon_1,\varepsilon_2,\varepsilon_{12}\right)$ data lying on the failure surface.

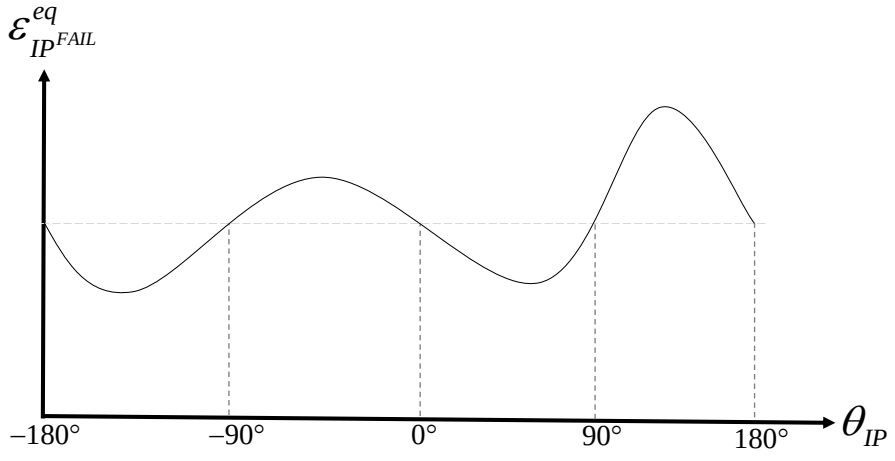

Figure 5. General form of in-plane failure surface [Shyamsunder et al., 2020b]

The equivalent strain, ε_{IP}^{eq} and failure angle, θ_{IP} can then be computed for each failure point as

$$\varepsilon_{IP}^{eq} = \sqrt{\varepsilon_{11}^2 + \varepsilon_{22}^2 + 2\varepsilon_{12}^2} \tag{25}$$

$$\theta_{IP} = \cos^{-1}\left(\frac{\sigma_{22}}{\sqrt{\sigma_{22}^2 + \sigma_{12}^2}}\right) \tag{26}$$

thereby permitting the creation of $\left(\varepsilon_{IP^{FAIL}}^{eq}, \theta_{IP}\right)$ input tabular data. Similarly, an out-of-plane failure surface can be constructed with $\left(\varepsilon_{OOP^{FAIL}}^{eq}, \theta_{OOP}\right)$ input tabular data with the values computed as

$$\varepsilon_{OOP}^{eq} = \sqrt{\varepsilon_{33}^2 + 2\varepsilon_{13}^2 + 2\varepsilon_{23}^2} \tag{27}$$

$$\theta_{OOP} = \cos^{-1}\left(\frac{\sigma_{13}}{\sqrt{\sigma_{13}^2 + \sigma_{23}^2}}\right) \tag{28}$$

During the finite element analysis, the failure detection at each Gauss point takes place as follows. First, the in-plane failure state e_1 is computed as

$$e_1 = \frac{\varepsilon_{IP}^{eq}}{\varepsilon_{IP^{FAIL}}^{eq}} \tag{29}$$

where, ε_{IP}^{eq} is computed for each Gauss point and time step and $\varepsilon_{IP^{FAIL}}^{eq}$ is what is specified as input failure surface. Similarly, the out-of-plane failure state e_2 is computed as

$$e_2 = \frac{\varepsilon_{OOP}^{eq}}{\varepsilon_{OOP^{FAIL}}^{eq}} \tag{30}$$

An element is eroded if $e \geq 1$ where

$$e = \begin{cases} \max(e_1, e_2) & if\ n = 0 \\ \sqrt[n]{(e_1)^n + (e_2)^n} & if\ n > 0 \end{cases} \tag{31}$$

where n is a user defined interaction parameter that can be used to couple the in-plane state of stress/strain to the out-of-plane state of stress/strain. The failure surfaces specified are used for predicting the element erosion rather than the failure onset.

Each stress-strain curve obtained from principal material direction/plane testing needs to be augmented to have a post-failure regime to handle the post-failure behavior via the damage sub-

model. It should be noted that handling the post-failure behavior correctly is crucial to obtaining a numerically stable solution since a finite element cannot be eroded (deleted) the instant peak stress is reached in the principal material direction/plane component. Fig. 6(a) shows a typical stress-strain input curve with a brittle failure where the post-failure data is added to experimentally obtained pre-peak data. The strain corresponding to peak stress is denoted ε^0, and ε^1 is the strain at the beginning of the residual strength regime in the post-failure region. Residual strength is expressed as a fraction (c^{RS}) of the peak stress that the material has when the element is finally eroded, i.e. $\sigma^f = c^{RS}\sigma^{\max}$, $0 \le c^{RS} \le 1.0$ (σ^f is the residual strength). There are a total of 9 residual strength parameters: $c_i^{RS}, i = 1,..,6$ for the normal tensile (1-3)/compressive (4-6) stresses in the PMDs, $c_i^{RS}, i = 7,8,9$ for the three principal shear components. For the deformation sub-model to carry out plasticity-related computations, the input stress in the effective stress space cannot have a negative slope. To ensure that this condition is satisfied, an effective damage parameter curve is used as input (Fig. 6(b)). This effective damage parameter data is computed for the respective component by keeping the effective stress constant and equal to the peak stress, $\sigma_{\max}$. Implementation details included a detailed algorithm can be found in our earlier publication [Shyamsunder et al., 2020b].

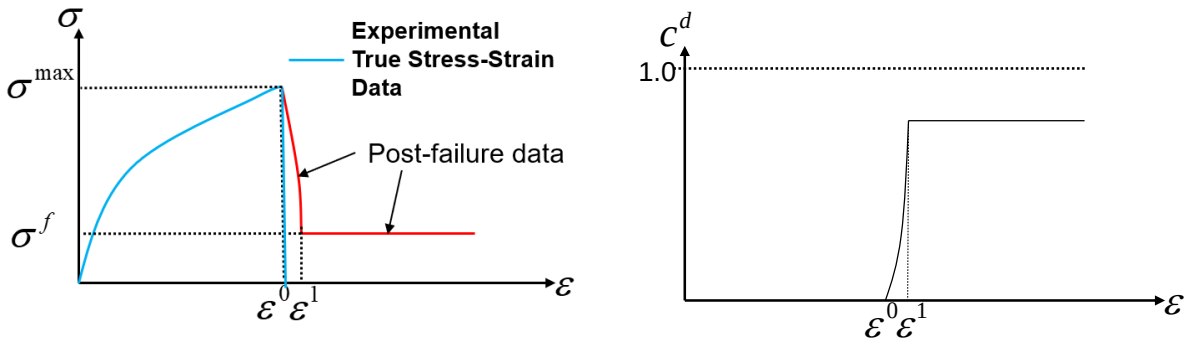

(a) (b)

Figure 6. (a) Stress-strain input augmented with post-failure data (b) Effective damage parameter input for handling post-failure behavior [Shyamsunder et al., 2020b]

Fig. 7(a) shows the post-failure augmented stress-strain curves for 2-direction tension. The figure also shows the 2-direction tension effective damage parameter curve (see secondary axis). In the current implementation, for each of the twelve stress-strain components only a single effective damage parameter curve can be used. This implies that for a given component, the effective damage parameter curve must be compatible with all the stress-strain curves. If there is no compatibility, there would be a numerical issue - plastic strain computed in the pre-processing step will turn out to be negative. The compatibility is maintained by making sure that all the stress-strain curves (3 in this case) have the same ultimate strain values. As can be seen in Fig. 1(a)/Fig. 7(a), *Model (325/s)* has the highest ultimate strain. Hence, the *Model (QS-RT)* and *Model (0.001/s)* are modified to have an additional data point with a stress value equal to the respective peak stress and a strain value equal to the ultimate strain of the *Model (325/s)* curve. The stress is gradually brought down to a residual strength of 30% of the respective peak stresses for all the 3 curves. The residual strength of 30% is a calibrated value obtained from the impact validation tests and is explained further in the numerical results section. Since the plasticity algorithm requires a non-

negative slope in the effective stress-effective plastic strain curve, the effective stress is kept constant as shown in Fig. 7(b).

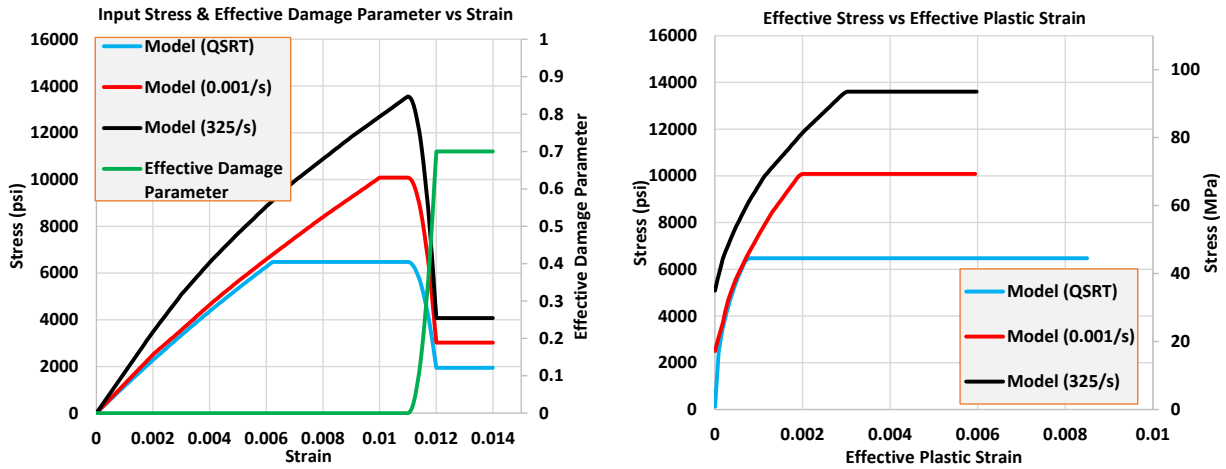

(a) (b)

Figure 7. 2-direction tension data for T800/F3900 composite (a) Input stress and effective damage parameter versus strain curves (b) Effective stress versus effective plastic strain curves constructed from data in (a)

3. Impact Test Setup and Protocol

Data for validating the model was obtained by conducting impact tests on flat composite panels according to the ASTM D8101 standard test method [ASTM, 2018] titled "Standard Test Method for Measuring the Penetration Resistance of Composite Materials to Impact by a Blunt Projectile". This test method is designed for measuring the response of composite materials under free-flight impact conditions when impacted in a normal direction. The test method utilizes a flat composite panel specimen whose thickness is small compared to its lateral dimensions. The specimen is clamped with 28 bolts between two thick metal plates with a 10-inch (25.4 cm) diameter circular aperture, as shown in Fig. 8(a). The test utilizes a cup-shaped aluminum 2024 projectile with a complex radiused nose and a mass of 1.77 oz (50 g). A cross-section of the projectile is shown in

Fig. 8(b). The projectile is accelerated toward the test specimen in a normal direction, typically with a single stage gas gun (Fig. 9).

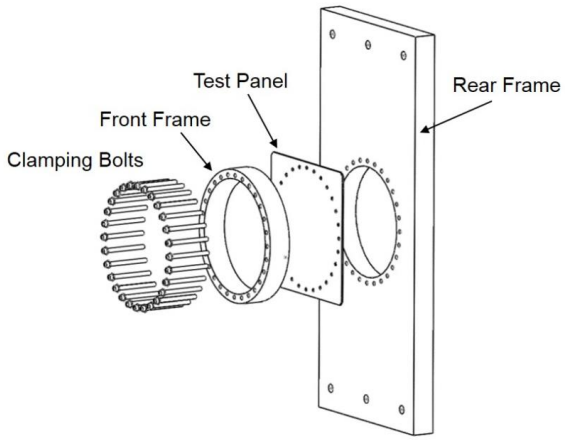

Figure 8(a). Schematic of fixturing for test method ASTM D8101

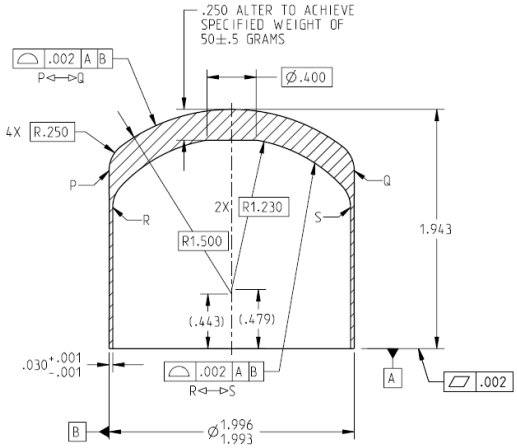

Figure 8(b). Cross section of standard projectile used in ASTM D8101 (dimensions in inches)

Figure 9. Single stage gas gun setup at NASA-Glenn Research Center

In this test series, the projectile was accelerated with the use of a single stage gas gun. The gun barrel had a length of 23.25 ft (7 m) and a bore of 2.00 inches (5 cm). The pressure vessel had a

volume of 1900 cubic inches. Fourteen tests were conducted at velocities that spanned the range from no detectable non-destructive inspection (NDI) damage to full penetration by the projectile. The test articles were Toray® T800/F3900 laminated angle-ply composites with a 16-ply $[[(0/90/45/-45)_2]_S$ layup.

Pairs of high-speed cameras and digital image correlation (DIC) software were used to compute the full-field displacements on both the front (impacted side) and rear of the specimen. Additionally, two pairs of cameras were located forward and behind the test specimen to measure the projectile velocity and orientation (pitch and yaw) before and after impact using photogrammetry software. The projectile orientation was specified by a set of three Euler angles (roll, pitch and yaw) about a local coordinate system fixed to the projectile. The coordinate system, in the un-rotated state, had an x-direction in the direction of the gun barrel, a y-direction horizontally to the right when looking at the front of the specimen, and a z-direction vertically downward. The roll angle was not reported due to the symmetrical nature of the projectile.

The front side DIC cameras operated at a rate of 40,000 frames per second (fps) with a resolution of 384x320 pixels per inch in horizontal and vertical direction respectively, and the rear side DIC cameras operated a rate of 80,000 fps with a resolution of 512x424 pixels per inch in horizontal and vertical directions. Both pairs of photogrammetry cameras operated at a rate of 20,000 fps with a resolution of 608x200 pixels per inch in the horizontal and vertical directions. Due to the tumbling of the projectile after impact, only the absolute values of post-penetration or rebound velocities are reported.

For the purpose of validating the damage and failure components of the MAT_213 model, only the four highest velocity tests from the series were used. Table 1 lists the test conditions.

Table 1. Validation impact test conditions

	Specimen	Projectile					Result
Test ID	**Panel Thickness in inches (cm)**	**Mass in grams**	**Impact Velocity in ft/s (m/s)**	**Post-Impact Velocity in ft/s (m/s)**	**Pitch Angle in degrees**	**Yaw Angle in degrees**	
LVG1075	0.122 (0.3)	49.65	385.0 (117.3)	-46.4 (-14.14)	0.08	-1.4	Rebound
LVG1074	0.122 (0.3)	49.96	417.0 (127.1)	25.4 (7.7)	0.38	-2.7	Penetration
LVG1076	0.122 (0.3)	49.55	453.3 (138.2)	114.3 (34.8)	-0.69	-1.2	Penetration
LVG1063	0.122 (0.3)	49.84	534.8 (163)	262.9 (80.1)	0.45	-0.4	Penetration

Computation of Strains and Strain Rates: The tests considered in this study involved impact velocities near to or above the threshold penetration velocity for the test specimens. As a result, there was considerable damage or penetration in all cases, causing a loss of the paint speckle pattern used for computing deformations in the region of the impact location. Therefore, deformations and strains could not be computed at the impact point soon after impact. However, it was evident that, for the short period when they could be computed, deformations, strains and strain rates where highest at the impact location itself.

4. Numerical Results

The developed constitutive model is used to model the four tests discussed in the earlier section. Two major components of the FE models used are described in detail in this section – (a) the

material data for various materials used in describing the various parts of the model, and (b) the finite element types and mesh, and boundary conditions.

Material Data: Two material models were used – MAT_213 for the composite panel and MAT_024 for the aluminum projectile. MAT_213 requires at least 12 QS-RT stress-strain curves [Khaled et al., 2017]. Two sets of simulations were carried out – (1) rate-independent cases which uses only the aforementioned 12 QS-RT stress-strain curves (2) rate-dependent cases which uses in addition to the QS-RT curves, the following stress-strain curves at room temperature: (a) 2-direction tension at 10^{-3}/s and 325/s, (b) 2-direction compression at 10^{-3}/s, 1/s and 813/s, and (c) 3-direction compression at 800/s [Deshpande et al., 2019]. FILT=0.0 in Eq. 7 since no numerical instabilities were detected. A numerical calibration process was used to estimate the decay constants β_{ij} (Eqns. 8 and 9) and a uniform value of 0.001 was found to be a suitable value for modeling the short-duration impact events considered in the paper.

FE Model: A detailed mesh convergence study was carried out to find an optimal mesh with a view to satisfactorily balance accuracy and computational time [Achstetter et al., 2020]. The element aspect ratio, number of elements in the through-thickness direction, hourglass control, and the element integration order were varied to gage the effect of each parameter on the maximum out-of-plane displacement and the time at which the maximum displacement occurred. These two computed values were compared against the experimental results. Based on the study, the following FE model parameters were selected for use in this paper: (a) 8-node reduced integration hexahedral elements were used to model the panel and the projectile, (b) each ply in the panel was modeled using one element through the thickness, and (c) while the results were not sensitive to different hourglass control, viscous hourglass control (IHQ=1) led to low hourglass energy values

and hence was used. The optimal mesh used in the simulations has a total of 91,728 elements to model the panel, and 17,040 elements to model the projectile. It should be noted that solid elements are appropriate for modeling this structure since the small diameter of the impactor compared to the total thickness of the target plate could cause out-of-plane shear failure which cannot be modeled with shell elements. Two points marked on the back side of the panel (Fig. 10) were used for the comparison of strain-rates with the experimental data. These points are chosen since experimental data were available at these points.

The nodes at the location of the bolts are restrained in-plane (Fig. 11(a)), and the nodes at the clamps were restrained in the out-of-plane direction (Fig. 11(b)). Eroding single surface (*CONTACT_ERODING_SINGLE_SURFACE) and eroding surface-to-surface (*CONTACT_ERODING_SURFACE_TO_SURFACE) control cards were used. The numerical examples use the deformation, damage and the failure sub-models in MAT_213.

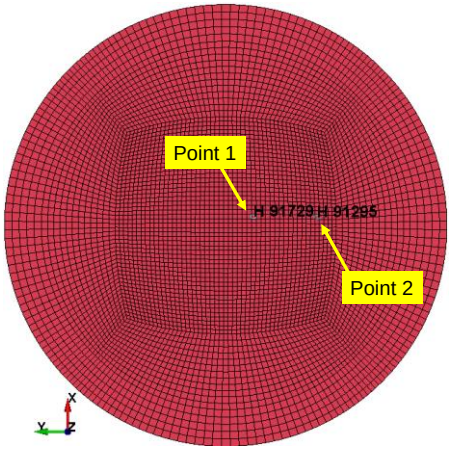

Figure 10. FE model used for the simulation

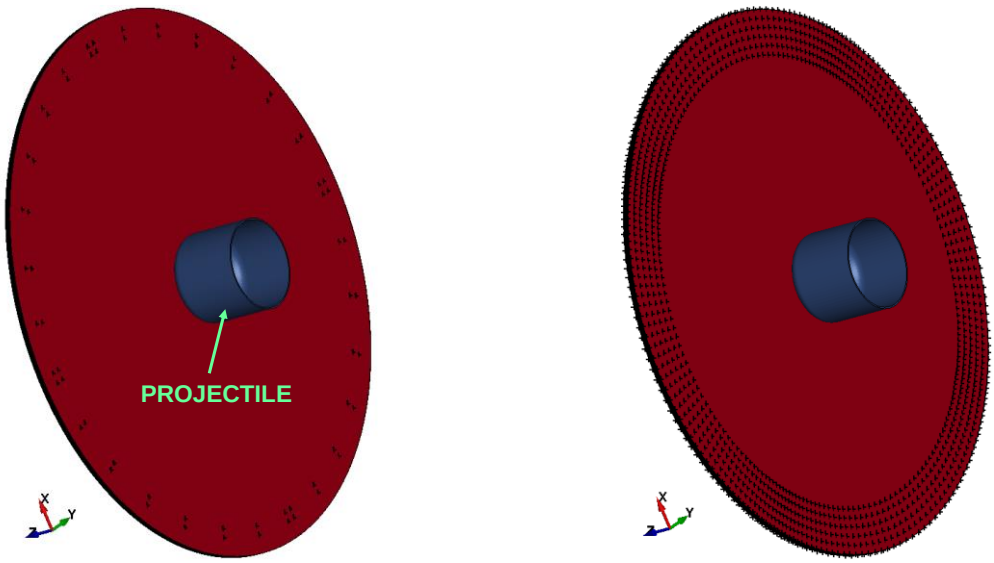

(a) (b)

Figure 11. Nodes which have translational restraints: (a) in-plane displacement (b) out-of-plane displacement

Calibration of the Residual Strength Values: While all other input to MAT_213 were obtained from experimental data, the residual strength parameters need to be calibrated since these parameters are not directly linked to any experimental data. To aid in the calibration process, a sensitivity analysis was carried out with three sets of failure parameters that are not directly related to experimentally obtained data. The in-plane residual strength $\left(c_1^{RS} = c_2^{RS} = c_7^{RS}\right)$, out-of-plane residual strength $\left(c_3^{RS} = c_8^{RS} = c_9^{RS}\right)$ and equivalent failure strain $\left(\varepsilon_{IP^{FAIL}}^{eq} = \varepsilon_{OOP^{FAIL}}^{eq}\right)$ were varied, and the exit/rebound projectile velocities were monitored. It was observed that the out-of-plane residual strength values most significantly affect the projectile exit/rebound velocity. As we will show later, this is also evident from Fig. 14 where it can be seen that the out-of-plane failure state values are higher than the corresponding in-plane values. A projectile impacting a plate perpendicularly is likely to show that the through-thickness failure is the dominant mode of failure. Thus, increasing the out-of-plane residual strength would make the panel stiffer and stronger, and thereby decrease the exit velocity or increase the rebound velocity. While the calibration exercise could have been

done with all the four test cases, the lowest velocity uncontained test (LVG1074) was chosen as this is the test with the impact velocity that is closest to V_0, the threshold penetration velocity. In the absence of experimental data, it was assumed that the two equivalent failure strains are equal $\left(\varepsilon_{IP^{FAIL}}^{eq} = \varepsilon_{OOP^{FAIL}}^{eq} = 0.80\right)$ and are a constant function of the failure angle. The interaction term, n was taken as 2 to couple the in-plane and the out-of-plane states of stress that are expected in an impact event. All the compression residual strength parameters were set equal to the respective peaks in the stress-strain input curves, $c_i^{RS} = 1.0, i = 4,5,6$, and the in-plane values as 30% of the peak values: $c_1^{RS} = c_2^{RS} = c_7^{RS} = 0.3$. Hence, with the objective of matching the FE simulation final (rebound) velocity to the experimental value, the only parameters that were obtained through a simple trial-and-error procedure were the out-of-plane components that were collectively (this was taken as a one-parameter calibration exercise) found to be 15%: $c_3^{RS} = c_8^{RS} = c_9^{RS} = 0.15$.

Results: The projectile exit/rebound velocity are shown in Fig. 12. The rate-dependent simulations and the rate-independent simulations are represented by the suffixes *MAT_213-W RATE* and *MAT_213-W/O RATE,* respectively. In this figure, a positive residual velocity implies a penetration of the projectile, and a negative residual velocity implies a rebound. The qualitative comparison of the crack patterns is shown in Fig. 13. It must be noted that the crack patterns shown are captured at the last frame from each simulation corresponding to the last point in Fig. 12. Table 2 shows the exit/rebound velocity error with respect to the experimental values. It also shows the normalized energy absorbed based on the kinetic energy and the difference with respect to the experimental values. Fig. 14 shows e_1 and e_2 contours on the back side of the panel. These images were captured at the same point of time for each of the test cases when e_1 and e_2 values were significantly large

before large through cracks were formed. The results shown in Figs. 13, 14, 15, 16, 17 and Table 2 correspond to the rate-dependent simulations.

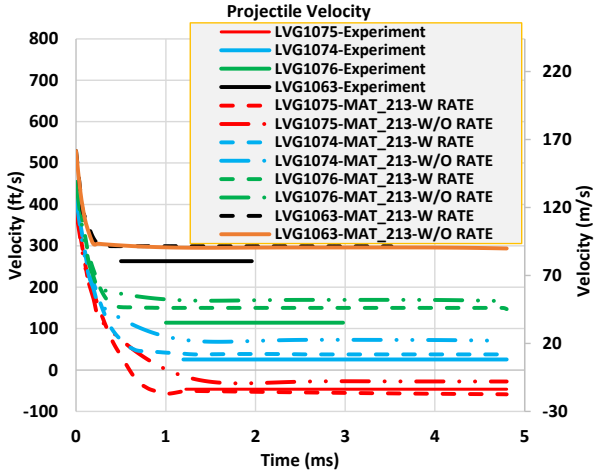

Figure 12. Comparison of projectile velocity for the impact tests

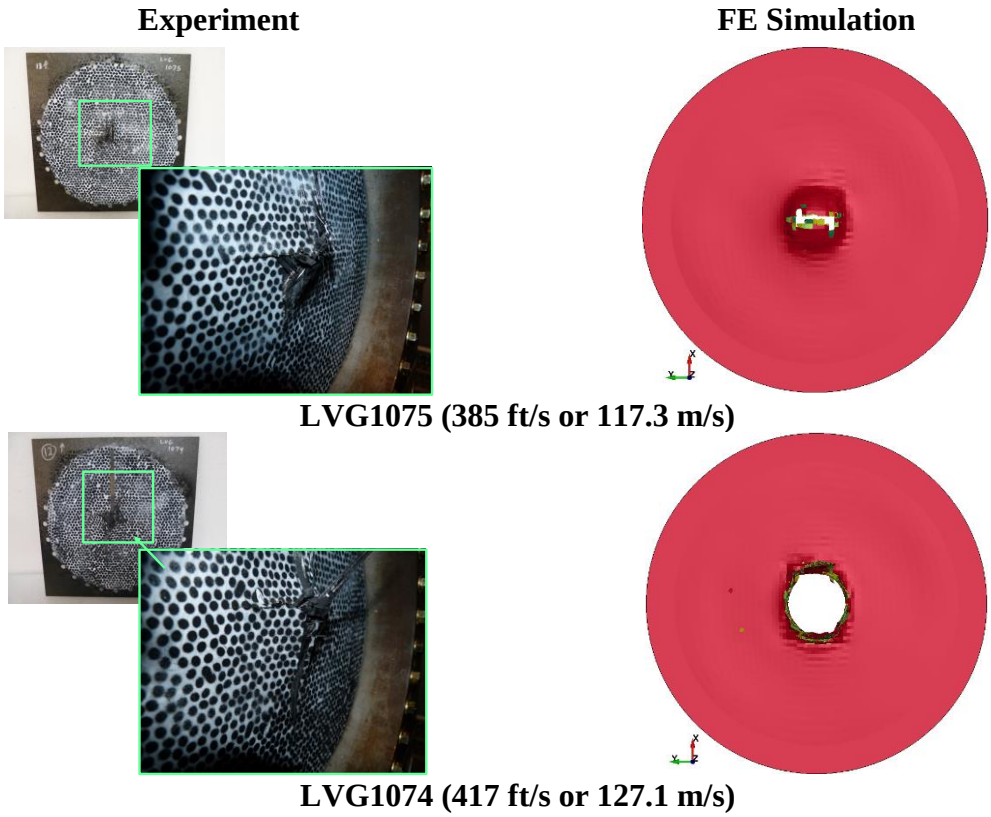

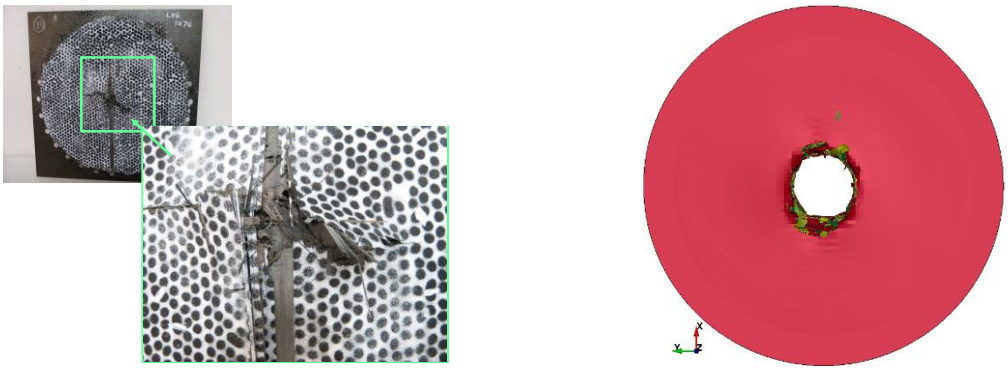

LVG1076 (453.3 ft/s or 138.2 m/s)

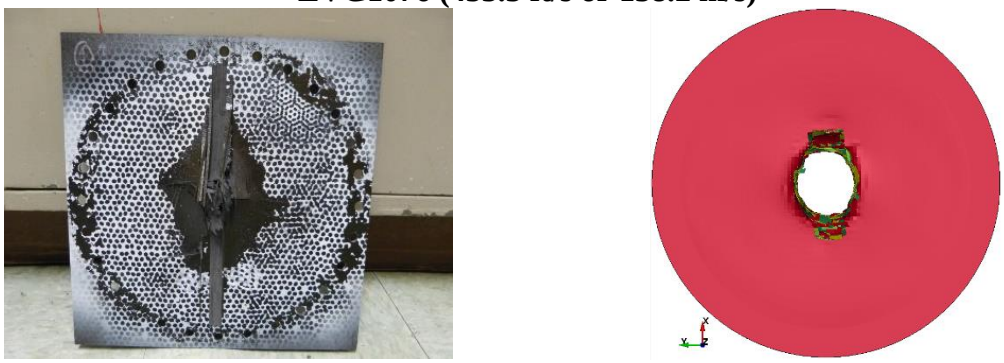

LVG1063 (534.8 ft/s or 163 m/s)

Figure 13. View of the back side of the tested composite panels and from last frame of the FE simulation

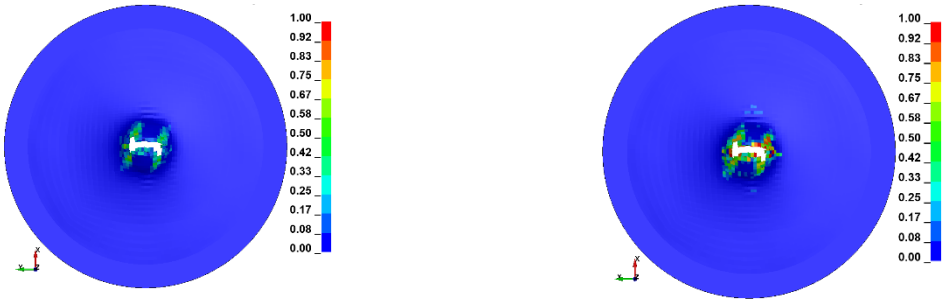

e_1 e_2

LVG1075 (385 ft/s or 117.3 m/s)

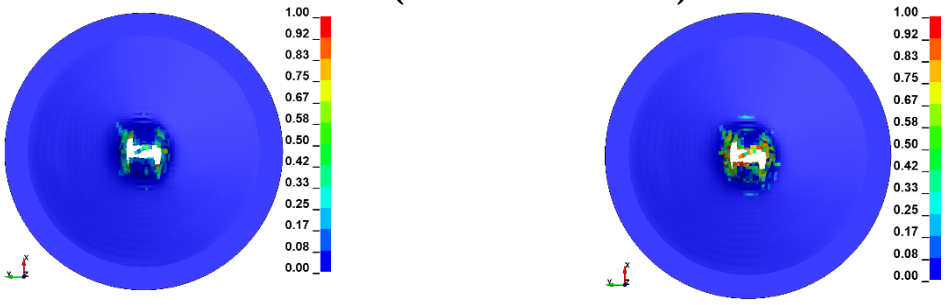

e_1 e_2

LVG1074 (417 ft/s or 127.1 m/s)

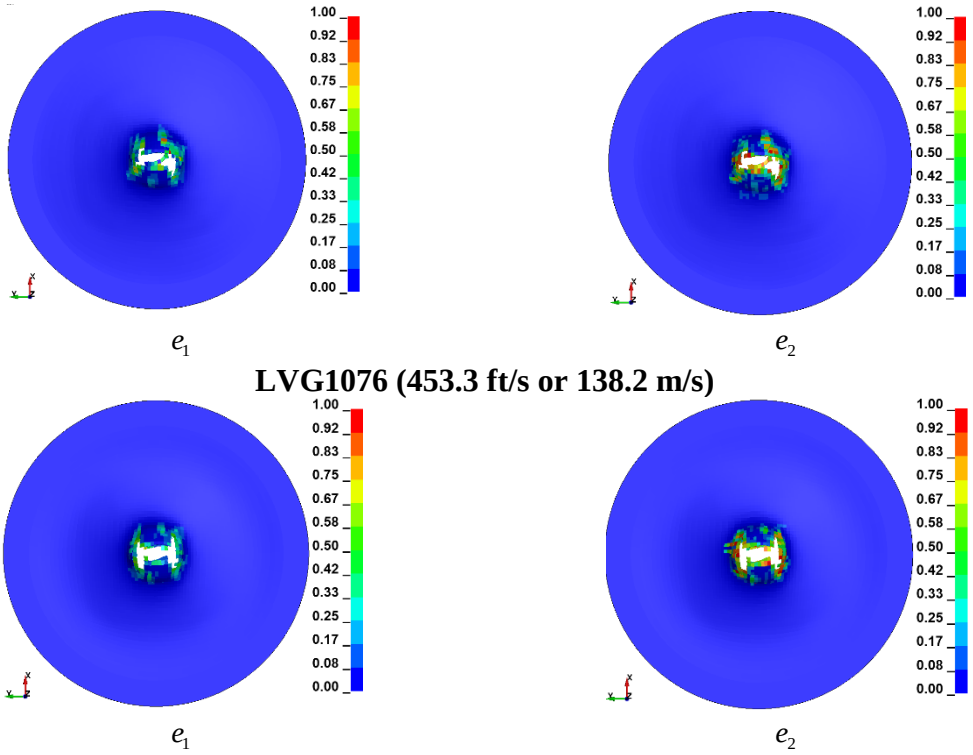

Figure 14. FE simulation generated in-plane e_1 and out-of-plane e_2 failure state contours on the back side of the panels

Table 2. Impact validation tests: FEA vs Experiment comparison

Test	**Impact Velocity, V_{IMP} in ft/s (m/s)**	**Final Velocity, V_f in ft/s (m/s)**			**Normalized Absorbed Energy $\left(\frac{V_{IMP}^2 - V_f^2}{V_{IMP}^2}\right)$**		
		Exp.	**FEA**	**Diff. (%) $\left(\frac{FEA - Exp}{Exp}\right)$**	**Exp.**	**FEA**	**Diff. (%) $FEA - Exp$**
LVG1063	534.8 (163)	262.9 (80.1)	300.0 (91.4)	14	0.75	0.68	-7
LVG1076	453.3 (138.2)	114.2 (34.8)	150.0 (45.7)	31	0.94	0.89	-5

LVG1074	417 (127.1)	25.4 (7.7)	37.6 (11.5)	48	0.99	0.99	0
LVG1075	385 (117.3)	-46.4 (-14.14)	-58.8 (-17.9)	26	0.99	0.98	-1

Discussion: The presence of rate-dependent stress-strain curves make the panel response stiffer compared to the rate-independent counterpart (Fig. 12) for all tests except LVG1063. In the LVG1063 simulation, the strain-rates in the panel during the impact are much higher (e.g., ~10^4/s in 2-direction tension/compression components) than the highest input rate-dependent stress-strain curve. Overall, considering all the rate-dependent simulations, the prediction of the projectile exit/rebound velocities are closer to the experimental results compared to the models where rate data has not been used. With using just one-parameter calibration exercise with one model, the results show consistent conservative predictions for all the four tests. Other than LVG1075, the predicted crack patterns did not compare well to the experimental results. There are few major factors affecting this behavior. First, the mesh size affects the crack pattern since in the failure sub-model, there is no mesh regularization technique. Second, as discussed earlier, there are no rate data available for the 3-direction tension component or the shear components. It is likely that these behaviors are rate dependent. Fig. 15 shows the 1-3 shear strain rate for all the different plies at the instant when the projectile makes contact with the panel for the LVG1075 test. The 1-3 shear strain-rate magnitude is very high (in the order of 10^4) in some of the elements in the 0° ply. Fig. 16 shows the effective plastic strain rate contour at the same point of time as that the contours shown in Fig. 15. The effective plastic strain rate magnitudes in some of the elements (mostly at the center) are also in the order of 10^4 which is much higher than the input that are of the order of

551 10^2. Having additional rate dependent input stress-strain curve would probably help improve the
552 predictions. Third, the boundary conditions at and around the bolt holes play an important role. In
553 the current model, it appears as if they are not helping promote vertical cracks over the surface
554 area of the panel as seen in Fig. 13 for LVG1076 and LVG1063. This is also evident from Fig. 17
555 which shows the absolute values of the strain-rate in 1-direction component plotted against time
556 at Point 1 and Point 2 (see Fig. 10 for the location of these points). The strain is more localized at
557 the vicinity of the impact in the simulation compared to the experiment. At this stage, due to
558 absence of input stress-strain curves at different temperatures, it is not clear as to what effect the
559 additional temperature dependent stress-strain data would have on the accuracy of the predictions
560 since the increase in the temperature around the point of impact is likely to be small.
561

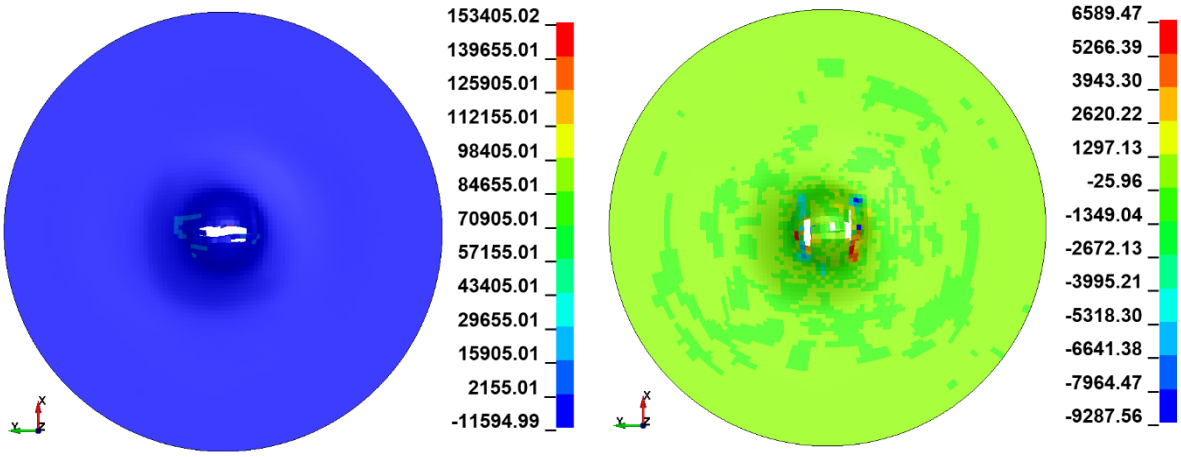

(a) (b)

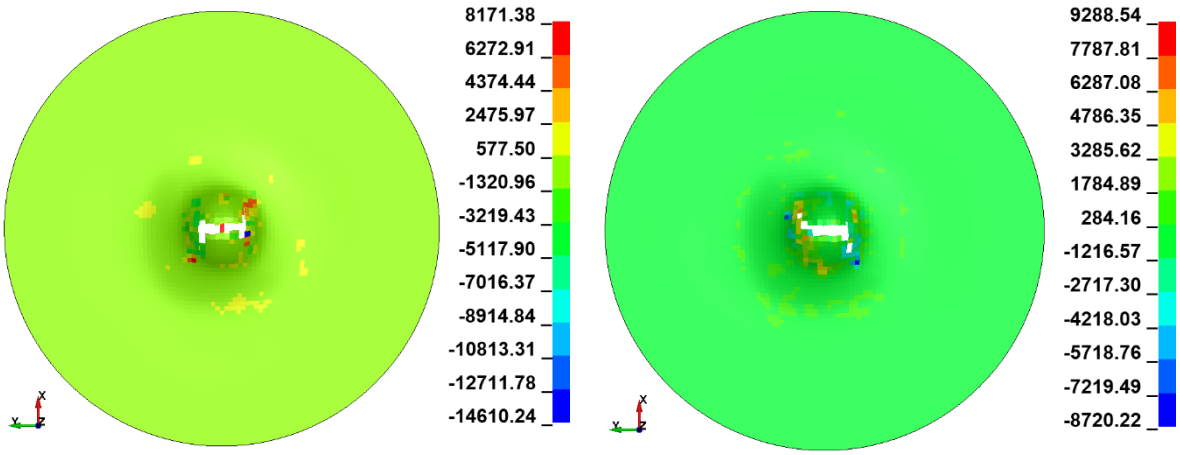

(c) (d)

Figure 15. Shear strain rate contour in the 1-3 plane from the LVG1075 simulation for (a) 0° plies (b) 90° plies (c) 45° plies and (d) -45° plies (view shown from back side of panel)

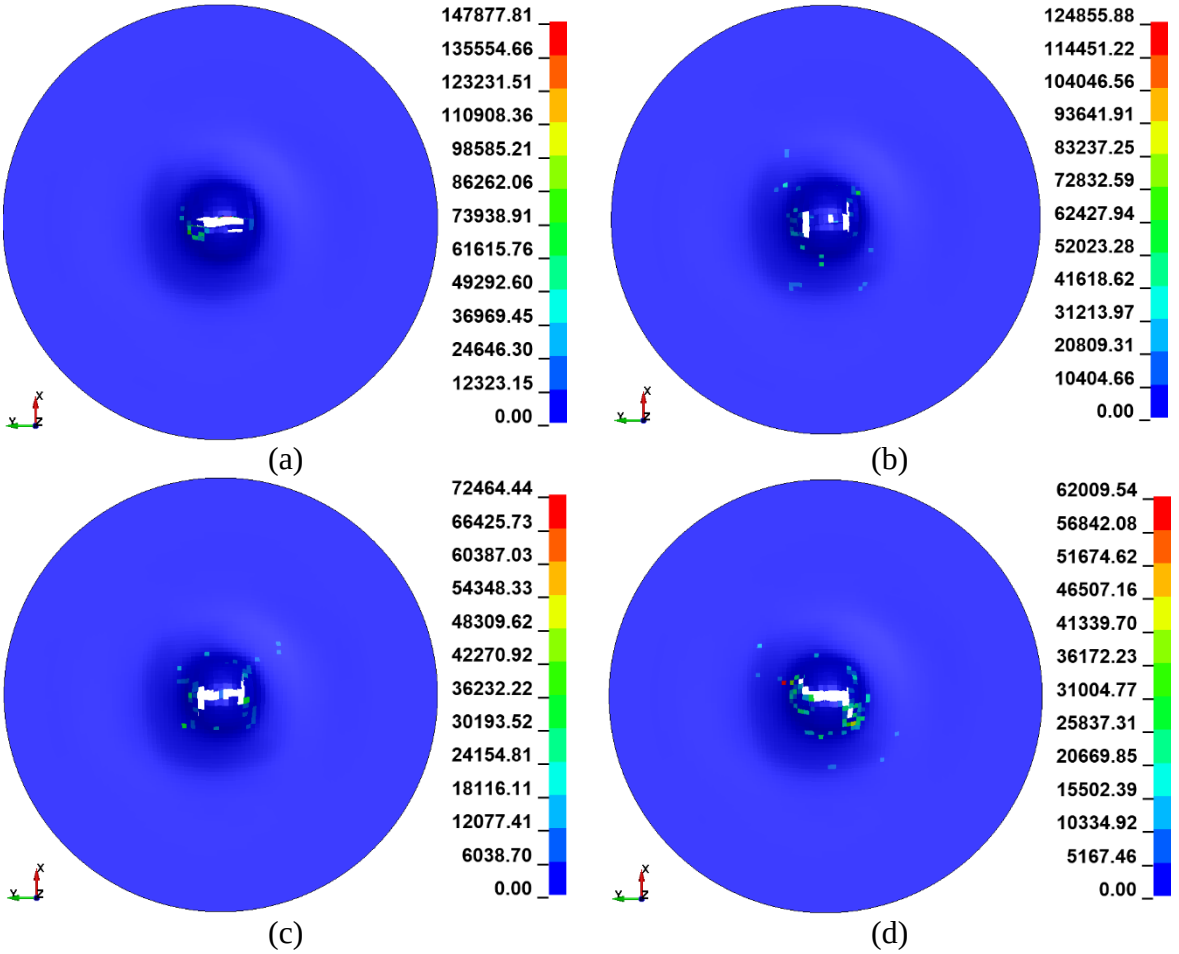

(a) (b)

(c) (d)

Figure 16. Effective plastic strain rate contour from the LVG1075 simulation for (a) 0° plies (b) 90° plies (c) 45° plies and (d) -45° plies (view shown from back side of panel)

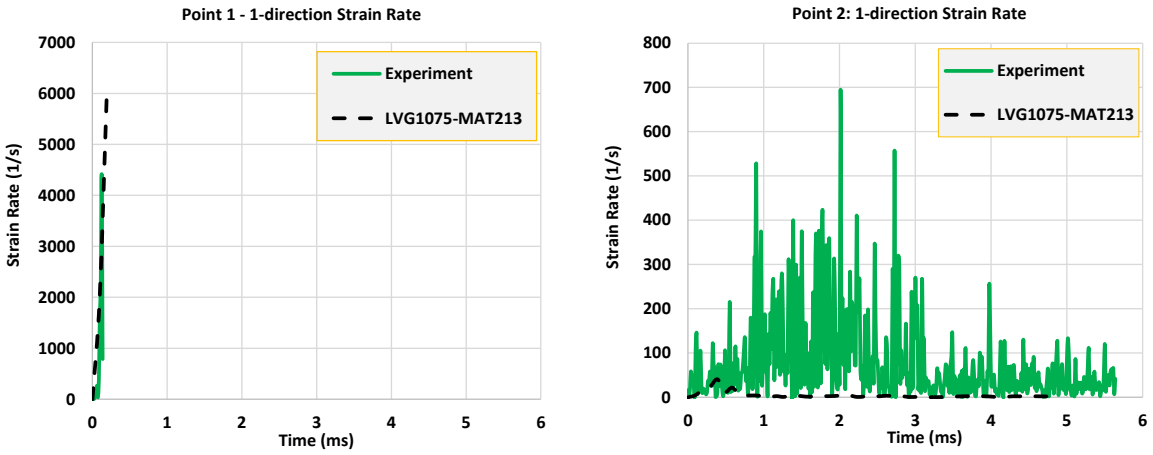

(a) (b)

Figure 17. Strain-rate in 1-direction (a) at point 1 (elements around point 1 are eroded quickly after impact) (b) at point 2 (see Fig. 10 for the location of point 1 and point 2)

5. Concluding Remarks

Details of a constitutive model that supports orthotropic visco-elastic-visco-plastic material behavior with temperature and strain rate dependence are presented in this paper. The constitutive model is implemented in LS-DYNA as *MAT_213 and has three sub-models supporting computations related to elastic and inelastic deformations, unloading and reloading, and detection of failure with the ability to erode the element from further computations. The focus is on (a) the development of VEVP behavior with rate and temperature dependence, (b) the processing the rate dependent curves to allow physically consistent predictions from FE analysis, and (c) using the Generalized Tabulated Failure Criterion to obtain numerically consistent failure predictions. A rich set of experimentally obtained impact validation data has been obtained from well instrumented tests that yield high fidelity data of the projectile as well as the impacted panel.

583 Tying a failure criterion to an explicit dynamics finite element analysis is difficult for a number of
584 reasons. First, is the challenge in detecting when an element has met the failure criterion. A
585 homogenized material model is typically deficient in its ability to differentiate between different
586 modes of composite failures since the architecture of the underlying composite is missing. Second,
587 most failure models have a large number of failure-related parameters, all of which are not easy to
588 obtain experimentally. The analyst must spend time not only understanding the role of these
589 parameters but also calibrating the values to obtain valid numerical responses. Third, each stress-
590 strain curve obtained from principal material direction/plane testing needs to be augmented to have
591 a post-failure regime so as to handle the post-failure behavior. This is required even if the
592 composite exhibits brittle and sudden failure. This post-failure behavior is crucial to obtaining a
593 numerically stable solution since a finite element cannot be eroded (deleted) the instant when the
594 failure criterion is satisfied.
595
596 Simulations of four ballistic impact test cases are presented. The difference between the predicted
597 normalized absorbed energy and the experimental data is less than 10% with excellent match for
598 the two lowest velocity tests (less than 1% difference). Consistently, the difference is conservative
599 with the difference increasing with increasing projectile velocity. The prediction of the crack
600 pattern of the panel could be improved. It should be noted that using cohesive zone elements
601 (CZEs) (LS-DYNA's MAT_186) to model inter-laminar failure based on our prior experimental
602 and modeling work [Khaled et al., 2019b] did not yield significant change in both the out-of-plane
603 displacement prediction as well as the crack pattern in the simulations discussed in this paper. As
604 stated earlier, it is likely that mesh size, the boundary conditions used, and lack of a complete suite

of rate-dependent stress-strain curves play a more important role. Efforts are underway to investigate these issues.

Acknowledgements

Authors Shyamsunder, Khaled and Rajan gratefully acknowledge the support of the Federal Aviation Administration through Grant #12-G-001 titled “Composite Material Model for Impact Analysis” and #17-G-005 titled “Enhancing the Capabilities of MAT213 for Impact Analysis”, William Emmerling and Dan Cordasco, Technical Monitors.

Conflict of Interest

None declared.

References

1. Achstetter T (2019). Development of a Composite Material Shell-Element Model for Impact Applications, *PhD Dissertation*, George Mason University, Fall 2019.
2. Achstetter T, Park C-K, and Kan C-D (2020). Development of a Tabulated Material Model for Composite Material Failure, MAT213. Part 3: Implementation of Probabilistic Modeling Capability in the Tabulated Composite Failure Model MAT213, *DOT/FAA/TC-19/50,P3*, Federal Aviation Administration, January 2020.
3. Ambur DR, Jaunky N, Lawson RE, and Knight Jr NF (2001). Numerical Simulations for High-Energy Impact of Thin Plates, *Intl J of Impact Engineering*, 25(7), 683-702.
4. Ansys-LST (2020). LS-DYNA Computer Program, http://lstc.com/, last accessed June 28, 2020.
5. ASTM D8101/D8101M (2018). Standard Test Method for Measuring the Penetration Resistance of Composite Materials to Impact by a Blunt Projectile, ASTM International, West Conshohocken, PA, DOI: 10.1520/D8101_D8101M-18.
6. Barbero, E. J. (2013). Finite element analysis of composite materials using ABAQUS, CRC Press, Boca Raton, FL.
7. Bhatnagar A (2016). Lightweight Ballistic Composites, Second Edition: Military and Law-Enforcement Applications, Woodhead Publishing Series in Composites Science and Engineering, London.
8. Chen X (2015). Advanced Fibrous Composite Materials for Ballistic Protection, Woodhead Publishing Series in Composites Science and Engineering, London.
9. Cho J, Fenner J, Werner B and Daniel IM (2010). A Constitutive Model for Fiber-reinforced Polymer Composites, *J Compos Mater*, 44-26, 3133-3150.

10. Chocron S, Carpenter AJ, Scott NL, Bigger RP, and Warren K (2019). Impact on Carbon Fiber Composite: Ballistic Tests, Material Tests, and Computer Simulations, *Intl J of Impact Engineering*, 131, 39-56.
11. Daniel IM, Werner BT, and Fener JS (2011). Strain-rate-dependent Failure Criteria for Composites, *Composites Science and Technology*, 71(3), 357-364.
12. Deshpande Y, Yang P, Seidt J, and Gilat A (2019). Dynamic Mechanical Response of T800/F3900 Composite under Tensile and Compressive Loading, *Proceedings of the 2019 Annual Conference and Exposition on Experimental and Applied Mechanics*, Reno, NV, June 2019.
13. DuBois P, Feucht M, Irsingler J, and Erhart T (2017). Implementation of a VE-VP Material Law for the Simulation of Energy Absorbing Thermoplastic Components, *11th European LS-DYNA Conference*, May 2017, Salzburg.
14. Goldberg RK, Carney KS, DuBois P, Hoffarth C, Harrington J, Rajan SD, and Blankenhorn G (2016). Development of an Orthotrpic Elasto-Plastic Generalized Composite Material Model Suitable for Impact Problems, *ASCE J Aerosp Eng*, 29(4). DOI: 10.1061/(ASCE)AS.1943-5525.0000580.
15. Goldberg RK, Carney KS, DuBois P, Hoffarth C, Harrington J, Rajan SD, and Blankenhorn G (2018). Analysis and Characterization of Damage Using a Generalized Composite material Model Suitable for Impact Problems, *ASCE J Aerosp Eng*, 31(4). DOI: 10.1061/(ASCE)AS.1943-5525.0000580.
16. Goldberg RK, Carney KS, DuBois P, Hoffarth C, Khaled B, Shyamsunder L, Rajan SD and Blankenhorn G (2018). Implementation of a Tabulated Failure Model into a Generalized Composite Material Model, *J Compos Mater*, 52(25), 3445-3460.

17. Hoffarth C, Rajan SD, Goldberg RK, Revilock D, Carney KS, DuBois P, and Blankenhorn G (2016). Implementation and Validation of a Three-Dimensional Plasticity-Based Deformation Model for Orthotropic Composites, *Composites A*, 91, 336-350.
18. Hoffarth C, Khaled B, Shyamsunder L, Rajan SD, Goldberg RK, Carney KS, DuBois P, and Blankenhorn G (2017). Verification and Validation of a Three-Dimensional Orthotropic Plasticity Constitutive Model Using a Unidirectional Composite, *Fibers*, 5(1), 1-13.
19. Khaled B, Shyamsunder L, Hoffarth C, Rajan SD, Goldberg RK, Carney KS, DuBois P and Blankenhorn G (2017). Experimental Characterization of Composites to Support an Orthotropic Plasticity Material Model, *J Compos Mater*, DOI: 10.1177/0021998317733319.
20. Khaled B, Shyamsunder L, Hoffarth C, Rajan SD, Goldberg RK, Carney KS, DuBois P, and Blankenhorn, G (2019a). Damage Characterization of Composites to Support an Orthotropic Plasticity Material Model, *J of Compos Mater*, 53(7), 941-967.
21. Khaled B, Shyamsunder L, Holt N, Hoover C, Rajan SD, and Blankenhorn, G (2019b). Enhancing the Predictive Capabilities of a Composite Plasticity Model using Cohesive Zone Modeling, *Composites A*, 121, 1-17.
22. Khan SA and Huang S (1995). Continuum Theory of Plasticity, John Wiley & Sons, New York.
23. Maimi, P, Camanho, PP, Mayugo, JA, and Davila, CG (2007). A continuum damage model for composite laminates. Part I: Constitutive Model, *Mech. Mater.*, 39(10), 897-908.
24. Matzenmiller, A.; Lubliner, J.; Taylor, R.L. (1995). A constitutive model for anisotropic damage in fiber-composites. *Mech. Mater*., 20, 125–152.

683 25. Melis ME, Pereira M, Goldberg R and Rassaian M (2018). Dynamic Impact Testing and Model
684 Development in Support of NASA's Advanced Composites Program. *AIAA Scitech 2018*
685 *Conference*, Kissimmee, FL.
686 26. Roberts G, Revilock DM, Binienda WK, Nie WZ, Mackenzie SB, and Todd KB (2002).
687 Impact Testing and Analysis of Composites for Aircraft Engine Fan Cases, NASA/TM-2002-
688 211493.
689 27. Shaktivesh NSN, Sesha Kumar CV, and Naik NK (2013). Ballistic Impact Performance of
690 Composite Targets, *J of Impact Engineering*, 51, 833-846.
691 28. Shyamsunder L, Khaled B, Rajan SD, Goldberg RK, Carney KS, DuBois P, and Blankenhorn
692 G (2019). Implementing Deformation, Damage and Failure in an Orthotropic Plastic Material
693 Model, *J of Compos Mater*, DOI: 10.1177/0021998319865006.
694 29. Shyamsunder L, Khaled B, Rajan SD, Carney KS, DuBois P, and Blankenhorn G (2020a).
695 Enhancement of Deformation sub-model in an Orthotropic Material Model, *Sixteenth LS-*
696 *DYNA User's Conference*, Detroit, Michigan.
697 30. Shyamsunder L, Khaled B, Rajan SD, and Blankenhorn G (2020b). Improving Failure Sub-
698 models in an Orthotropic Plasticity-based Material Model, *J of Compos Mater*, DOI:
699 10.1177/0021998320982651.
700 31. Stahlecker Z, Mobasher B, Rajan SD, and Pereira JM (2009). Development of Reliable
701 Modeling Methodologies for Fan Blade-Out Containment Analysis. Part II: Finite Element
702 Analysis, *J of Impact Engineering*, 36(3), 447-459.
703 32. Sun, C.T.; Chen, J.L. (1989). A Simple Flow Rule for Characterizing Nonlinear Behavior of
704 Fiber Composites. *J. Compos. Mater.*, 23, 1009-1020.

33. Toray Carbon Fibers America (2020). https://www.toraycma.com/ (last accessed June 28, 2020).
34. Vaziri, R.; Olson, M.D.; Anderson, D.L. (1991). A Plasticity-Based Constitutive Model for Fibre-Reinforced Composite Laminates. *J. Compos. Mater.*, 25, 512-535.
35. Wang WM, Sluys LJ, and De Borst, R (1997). Viscoplasticity for Instabilities due to Strain Softening and Strain-rate Softening, *Intl. J of Numerical Methods in Engineering*, 40(20), 3839-3864.
36. Wu, F.; Yao, W. (2010). A fatigue damage model of composite materials. *Int. J. Fatigue*, 32, 134-138.

Declaration of interests

☒ The authors declare that they have no known competing financial interests or personal relationships that could have appeared to influence the work reported in this paper.

☐The authors declare the following financial interests/personal relationships which may be considered as potential competing interests:

Author Statement "*Numerical Validation of Composite Panel Impact Tests"*

Loukham Shyamsunder: Methodology, Software, Validation, Writing – Original Draft, Data Curation.

Bilal Khaled: Methodology, Software, Resources, Investigation, Data Curation.

Subramaniam D. Rajan: Methodology, Supervision, Project Administration, Funding Acquisition, Writing – Review and Editing.

J. Michael Pereira: Validation, Investigation, Data Curation, Writing – Review and Editing.

Paul DuBois: Conceptualization, Methodology, Writing – Review and Editing.

Gunther Blankenhorn: Software, Data Curation.